Experimental investigation of the angle of attack dependence of the flow past a cactus-shaped cylinder with four ribs

Oleksandr Zhdanov[a,*], Richard Green[a], Angela Busse[a]

[a] *James Watt School of Engineering, University of Glasgow, Glasgow G12 8QQ, United Kingdom*

Abstract

The aerodynamic properties of a two-dimensional cactus-shaped cylinder with four ribs are studied experimentally. The cross-section of the cylinder corresponds to a modified square cylinder with rounded corners and concave sides inspired by tall succulents with four ribs. The mean aerodynamic coefficients, fluctuating lift coefficient, Strouhal number, and mean surface pressure distribution are measured as a function of the angular orientation for Reynolds numbers ranging from 50,000 to 150,000. Hot-wire measurements are conducted at two locations in the wake for several angles of attack to provide insight into the vortex shedding frequencies. The results show that the studied shape exhibits a strong angle of attack dependence while no Reynolds number dependence is found within the tested range. As for the square cylinder, a critical angle of attack of approximately 13° is observed at which drag and fluctuating lift forces are minimised while mean lift and Strouhal number reach their highest values. Reattachment of the shear layer at and above the critical angle of attack is confirmed using PIV. Overall, succulents with four ribs retain some of the aerodynamic benefits that have been observed for cactus-shaped cylinders with many ribs, albeit over a limited range of angles of attack.

Keywords: bluff body, cactus-shaped cylinder, square cylinder, nature inspired

1. Introduction

Flow past bluff bodies has been a long-standing subject of fluid mechanics research due to its numerous practical applications in engineering. Bluff bodies, especially circular and square cylinders, are very common shapes that are present in various structures (e.g. tall buildings, suspension bridges, risers, heat exchangers). It is well known that the aerodynamic characteristics as well as the

*Corresponding author
E-mail address: o.zhdanov.1@research.gla.ac.uk (Oleksandr Zhdanov)

wake of the circular cylinder are strongly dependent on the Reynolds number ($Re = U_\infty D/\nu$, where U_∞ is freestream velocity, D is the cylinder diameter, and ν is the kinematic viscosity of the fluid). With increasing Reynolds number the location of the separation points on the cylinder surface changes and four distinctive flow regimes, namely subcritical, critical, supercritical and transcritical exist (see e.g. Achenbach (1971)).

In contrast, for the square cylinder, the separation points are fixed at the leading edge corners and its aerodynamic behaviour does not depend on Reynolds number for $Re > 1,000$ (see e.g. Bai and Alam (2018)). While the circular cylinder is insensitive to angular orientation due to its symmetry, strong angle of attack (α) dependence is observed for flow past the square cylinder. The general convention applied for the angle of attack definition is that the 0° case is when the freestream is normal to a side of the cylinder and maximum angle of attack (45° case) is attained when one of the corners of the square cylinder is facing the flow. One of the distinctive features of the angle of attack dependence of the square cylinder is the presence of a critical angle of attack (α_{cr}), at which the shear layer that separates from the front corner reattaches to the side face of the cylinder (Lee, 1975). As a result of the reattachment, minimum values of drag and fluctuating lift coefficients together with maximum Strouhal number and absolute lift coefficient are observed at this angle of attack. Flow patterns around the square cylinder also change with angular orientation and can be subdivided into two main regimes, the perfect separation and reattachment flow regimes, separated by the critical angle of attack (Igarashi, 1984).

Various drag reduction and passive flow control techniques have been applied to circular and square cylinders. Splitter plates placed along the wake centreline alter vortex shedding and reduce drag of both circular (Apelt et al., 1973) and square cylinders (Bearman and Trueman, 1972). Another way to reduce drag of the square cylinder is through corner modifications. Naudascher et al. (1981) studied the influence of recessed corners on the mean aerodynamic forces. Experimental investigations were carried out for square-shaped recesses of two different sizes. Both configurations provided drag reduction over the full angle of attack range, and decrease in the lift force was observed at most angular orientations.

Tamura and Miyagi (1999) investigated the effect of rounded and chamfered corners on the flow past square cylinders. Both modifications reduce the aerodynamic drag experienced by the square cylinder over all reported angles of attack. However, a reduction of the lift force and its fluctuations was observed only at some angular orientations. With the increase of the freestream turbulence intensity this trend was sustained but the difference in lift force fluctuations between the standard square cylinder and those with modified corners was reduced compared to uniform inflow. In addition, a decrease in the critical angle of attack was observed as result of the corner modifications.

A square cylinder can be transformed into a circular cylinder by increasing the radius of corner rounding. An experimental study on a set of cylinders with various corner roundings at zero angle of attack was conducted by Hu et al. (2006). Their results show that as a square is morphed into a circular cylinder,

mean drag decreases while an increase in Strouhal number is observed. Carassale et al. (2014) studied the angle of attack dependence of square cylinders with two different corner roundings. Both studied modifications showed an increase in Strouhal number compared to the square cylinder for all angles of attack. On the other hand, it was reported that small corner rounding leads to reduction of drag only below the critical angle of attack. For the higher corner rounding drag reduction was observed for all angular orientations. In addition, it was shown that while rounded corners reduce the fluctuating lift coefficient at angles of attack below critical, an increase was observed for angles of attack above α_{cr}. As in the case of other corner modifications, a reduction of the critical angle of attack was found for both cylinders with rounded corners.

He et al. (2014) investigated the effect of another type of corner modification by recessing the corners of the leading edge of a square cylinder. At zero angle of attack, drag reduction was achieved for all studied configurations of rectangular recesses. However, drag was found to be dependent on the size and orientation of the recesses. Rectangular recesses where the longer side was aligned with the direction of the flow provided higher drag reduction compared to the same recesses where the longer side was normal to the freestream direction. As for other types of corner modifications, an increase in Strouhal number compared to the square cylinder was observed.

The natural world has been a source of inspiration for a number of drag reduction and passive flow control approaches including modifications to the cross-sections of bluff bodies (Bushnell and Moore, 1991; Choi et al., 2012). For example, Hanke et al. (2010) and Wang and Liu (2016) showed that a cylinder shape inspired by the vibrissae of harbour seals suppresses vortex-induced vibrations compared to a regular circular cylinder. Another modification to the cross-section of the circular cylinder has been inspired by the Saguaro cactus, a tall slender plant with ribbed, approximately circular cross section, that can have up to 30 ribs. Experimental and numerical investigations showed that the ribs on the cactus trunk help to reduce drag and the magnitude of unsteady force fluctuations (Talley et al., 2001; Cheng et al., 2018) compared to the smooth circular cylinder. In the plant kingdom, there are a number of tall, cactus-like succulents that have only four ribs, e.g. *Euphorbia abyssinica*, *Euphorbia ammak*, or *Euphorbia ingens*. Their cross sections resemble a square cylinder with concave sides and rounded corners. Taking into account that these succulents have developed their plant features, including ribs, independently from cacti through the process of convergent evolution (McGhee, 2011), their shape may provide aerodynamic benefits similar to those of cactus-shaped cylinders with many ribs. In a 2D URANS study it was found that a succulent-inspired cylinder with four ribs has superior aerodynamic behaviour compared to the regular square cylinder at certain angles of attack (Zhdanov and Busse, 2019).

In the present study, the aerodynamic properties of a succulent-inspired cylinder with four ribs are measured in a wind tunnel to investigate its ability to reduce drag and modify force fluctuations and Strouhal number. Force and surface pressure measurements were carried for 17 angular orientations ranging from 0° to 45° at Reynolds numbers $50,000$, $100,000$, $120,000$, and

150,000. Hot-wire measurements were performed in the wake at Reynolds number 100,000 to provide further insight into the vortex shedding frequencies. Flow visualisation was conducted using particle image velocimetry for a range of angular orientations at Reynolds number 50,000.

The current paper is organised into four sections: In Section 2 the details of the tested model and the experimental setup are described. The experimental results for mean force coefficients, fluctuating lift coefficient, mean surface pressure distribution, Strouhal number and hot-wire measurements in the wake are presented in Section 3. Finally, in Section 4 general conclusions on the ability of ribs to help tall succulents to cope with high wind loads are given.

2. Experimental setup

Force, surface pressure and wake hot-wire measurements were conducted in the low-speed deHavilland tunnel at the University of Glasgow, a closed-return type wind tunnel facility. The wind tunnel test section has a 2.66 m $\times$ 2.1 m octagonal cross-section and is 5.5 m long with 5 : 1 contraction ratio. Turbulence intensity in the empty test section is below 0.2%.

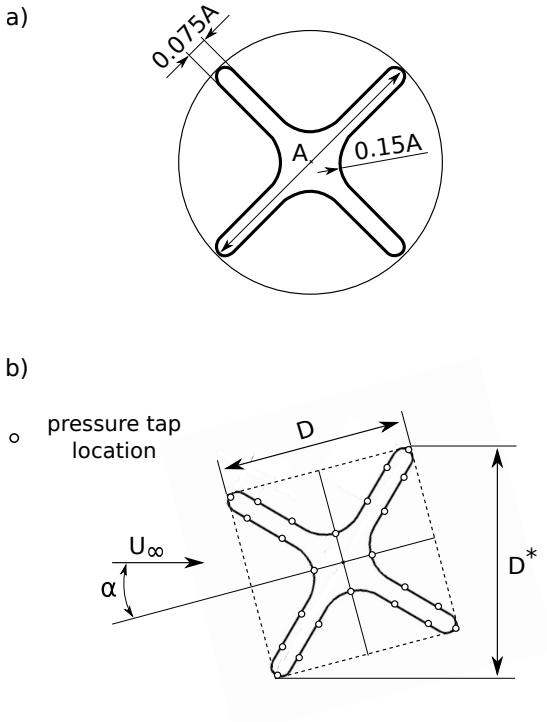

Figure 1: a) Geometrical representation of the studied geometry. b) Definitions of length scales, angle of attack, and location of the pressure taps on the model of the cactus-shaped cylinder with four ribs

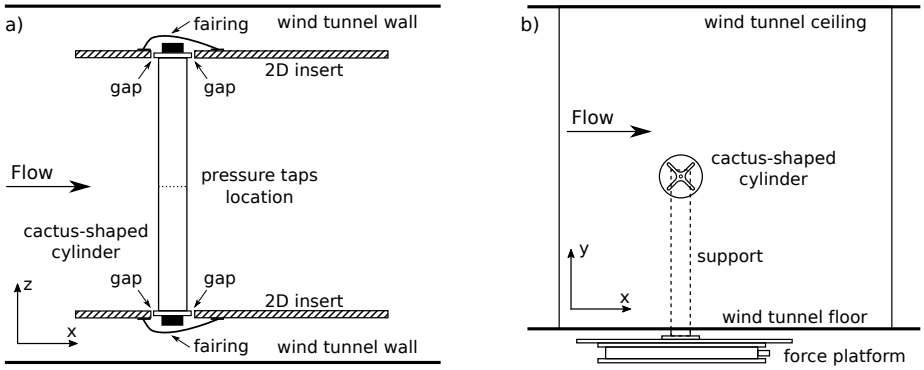

Figure 2: Schematic diagram of the experimental setup. a) Top view, showing 2D insert to the test section and location of pressure taps on the cactus-shaped cylinder model. b) Side view, showing force platform mounted beneath the wind tunnel test section

The tested model, a cactus-shaped cylinder with four ribs, is based on the succulent *Euphorbia abyssinica*. The plant's cross section was approximated using simple geometrical relations (Figure 1a). The model has a 3D printed central section, where pressure taps are installed. The end parts were made from model foam. To strengthen the model it was reinforced by a steel tube along its central axis. The surface of the model was painted and polished to give a smooth finish. The dimensions of the cactus-shaped cylinder model are $110 \times 110 \times 1250$ mm^3 (width $\times$ height $\times$ length). At zero angle of attack these dimensions give an aspect ratio of 11.4% and a blockage ratio of 5.16%. Blockage corrections were not applied to the experimental data, following the approach by Tamura and Miyagi (1999) for a 2D square cylinder with blockage ratio of 5% at $\alpha = 0°$.

To achieve two-dimensional flow conditions, a 2D insert was installed in the wind tunnel test section. The model was mounted horizontally between the walls of the 2D insert at approximately the mid-height of the wind tunnel test section (Figure 2).

The orientation of the model with respect to the incoming flow was varied manually and checked by a digital inclinometer at several positions along the model span. The angle of attack (α) definition was adopted from the square cylinder studies, namely zero angle of attack is when the flow is normal to the cavity of the cactus-shaped cylinder, while $\alpha = 45°$ when the rib tip is facing the flow (Figure 1b). In the present study data have been acquired at 17 angular orientations: 0°, 5°, 7.5°, 10°, 11°, 12°, 13°, 14°, 15°, 20°, 22.5°, 25°, 30°, 35°, 37.5°, 40°, and 45°. First, the measurements were carried out with 5° steps. Next, to increase resolution, the data was acquired with 7.5° steps excluding repetitive orientations. Finally, in the range $10° \leq \alpha \leq 15°$ the data was recorded with 1° steps to capture the critical angle of attack.

Wind tunnel dynamic pressure was measured with Pitot-static probe at the working section entry and using pressure tappings in the wind tunnel settling chamber and contraction. The experiments were conducted at four Reynolds

numbers, namely 50,000, 100,000, 120,000 and 150,000. The Reynolds number was based on the distance between adjacent rib tips (D), i.e. the length of the side of the equivalent square cylinder (Figure 1b).

2.1. Force measurements

The forces were measured by an AMTI OR6-7-1000 force platform, installed under the wind tunnel floor, at 1 kHZ rate for at least 100 s. This corresponds to a minimum of approximately 700 shedding cycles at the lowest tested Reynolds number of 50,000 in $\alpha = 45°$ configuration. The accuracy of the measurements is $\pm 0.25\%$ of the applied load. To eliminate interference between the model ends and the walls of the 2D insert they were separated by a small gap (see Figure 2a).

2.2. Pressure measurements

In the central plane of the cactus-shaped cylinder 24 pressure taps were installed. Pressure taps were located at the tip of each rib and at the centre of each cavity. In addition, each rib had 2 taps on each side (Figure 1b). All pressure taps were connected to a Scanivalve ZOC23b miniature pressure scanner (range ± 2.5 kPa) through PVC tubes. Surface pressure was determined at every measuring point as an average over 1600 data points. Resolution of the pressure scanner of around 1 Pa provided accuracy of the pressure coefficient close to 1%.

2.3. Hot-wire measurements

Hot-wire measurements were conducted using a Dantec Dynamics StreamLine Pro System with X-probe (55P61) at Reynolds number 100,000. The probe sensors are tungsten wires with diameter of 5 μm and length 1.25 mm. Data was sampled at 10 kHz rate for 60 s. Before and after each set of measurements the probe was calibrated using a StreamLine Pro automatic directional calibrator. The estimated accuracy of the hot-wire measurements is around 1% based on the results reported in Kawall et al. (1983).

2.4. PIV measurements

Quantitative flow visualisation was performed using two-dimensional, two-component particle image velocimetry (PIV) in a 1.15 m $\times$ 0.85 m low speed, closed-return wind tunnel with turbulence intensity of approximately 0.3% at the University of Glasgow (Green et al., 2005). The same model, as in the aforementioned experiments, was mounted in a cantilever configuration with model's axis spanning across the mid-height of the tunnel in the horizontal plane. The span of the model was adjusted to fit flush to both sides of the tunnel. The PIV measurements were performed around the model (indicated as PIV area 1 in Figure 3) at Reynolds number of 50,000 for six angular orientations, namely 0°, 5°, 10°, 13°, 15°, and 30°. In addition, for two orientations, 13° and 10°, i.e. at the critical angle of attack and at an angle just below, close up quantitative

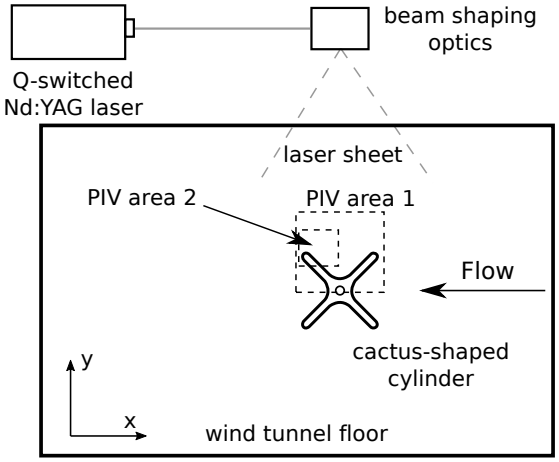

Figure 3: Schematic diagram of the experimental setup used for PIV quantitative visualisations of the flow over the top part of the cactus-shaped cylinder with four ribs

flow visualisations (indicated as PIV area 2 in Figure 3) were carried out to capture the reattachment of the separated shear layer.

Illumination for the PIV was provided by a Quanta-Ray, single cavity, Q-switched Nd:YAG pulsed laser with frequency doubler that produced a pulsed output of 8 ns duration with 532 nm wavelength. The laser was directed into the wind tunnel working section from above and expanded into a thin sheet using beam shaping optics and a cylindrical lens. The light sheet was in the vertical plane coincident with the lateral symmetry plane of the wind tunnel test section. A 10-bit, Redlake Megaplus 4 2048 $\times$ 2048 pixel CCD camera was used to capture images for the PIV, with each image synchronised with a laser Q-switch pulse. The camera was fitted with a selection of lenses for the PIV including an 85 mm focal length lens at $f/2$ for the PIV area 1 and a 200 mm focal length lens at $f/4$ for the PIV area 2. The PIV setup was spatially calibrated by taking a photograph of a grid of 2 mm diameter dots with a 5 mm pitch, and performing a least-squares fit to the centroids of the dot images. PIV seeding was generated by a Concept Systems Viscount fog generator that heated a light smoke oil (density 700 kg m^{-3}) and was pumped into the wind tunnel circuit using carbon dioxide. The notional seeding particle size was < 1 μm. The PIV inter-pulse time delay was set between 40 and 80 μs depending on the field of view, flow speed, and required accuracy and resolution for analysis. The field of view was set to 150 mm $\times$ 150 mm for the PIV area 1 and 50 mm $\times$ 50 mm for the PIV area 2. In total, 144 image pairs were recorded for each tested configuration.

Image analysis for the PIV was performed using the well-established cross-correlation technique with image shifting for improved accuracy and data validation and to avoid the peak-locking bias effect inherent in digital PIV. Correlation peak detection accuracy was improved to around 0.1 pixel by using a local Gaus-

sian fit. Image tile (sub-window) size was initially selected at 32 × 32 pixels and reduced to 16 × 16 pixels for higher spatial resolution where required. Use of this PIV system and image analysis technique has been reported in detail in Green et al. (2005). Spatial calibration error and PIV timing errors were negligible. The major source of error in the PIV was the digital bias, which itself was dependent upon the field of view. The maximum field of view used for this study (150 mm × 150 mm) gives an accuracy of around 2% at the wind tunnel speed that is required to attain a Reynolds number of 50,000 (approximately 8ms^{-1}). Spatial resolution according to vector spacing was around 1 mm × 1 mm.

3. Experimental results

3.1. Mean force coefficients

Mean drag and lift force coefficients of the cactus-shaped cylinder with four ribs were calculated from the experimental data as:

$$C_D = \frac{\overline{F}_D}{0.5\rho U_\infty^2 A}, \qquad C_L = \frac{\overline{F}_L}{0.5\rho U_\infty^2 A}, \tag{1}$$

where $\overline{F}_D$ and $\overline{F}_L$ are the measured mean values of drag and lift force respectively, ρ is the density of air determined based on the temperature inside the wind tunnel, and A is the projected frontal area of the cactus-shaped cylinder.

The mean drag and lift coefficients are presented as a function of angle of attack for the four tested Reynolds numbers in Figure 4. No significant Reynolds number dependence of the force coefficients is observed within tested range. On the other hand, both C_D and C_L show strong variation with the angle of attack. With an increase of α in the range from 0° to 13°, the drag coefficient decreases, reaching its minimum value at $\alpha = 13°$. With further increase of the angle of attack, a monotonic increase of the drag coefficient is observed.

An opposite trend is observed for the absolute value of the lift coefficient which increases with angle of attack from 0 at $\alpha = 0°$, where the mean flow around the cactus-shaped cylinder is symmetric, to its absolute maximum value at $\alpha = 13°$. At higher angles of attack the value of the lift coefficient decreases and returns to 0 at $\alpha = 45°$, where symmetry of the mean flow is restored.

Similar trends in the behaviour of the mean force coefficients with the increase of an angle of attack are observed in both cactus-shaped and square cylinders (Figure 4). However, compared to the square cylinder, a reduction of the drag coefficient is observed for the cactus-shaped cylinder at angles of attack up to 30° (Figure 4a). The absolute value of the lift force coefficient is higher for the cactus-shaped cylinder at all angles of attack, except for 0° and 45°, where zero lift is observed for both shapes (Figure 4b).

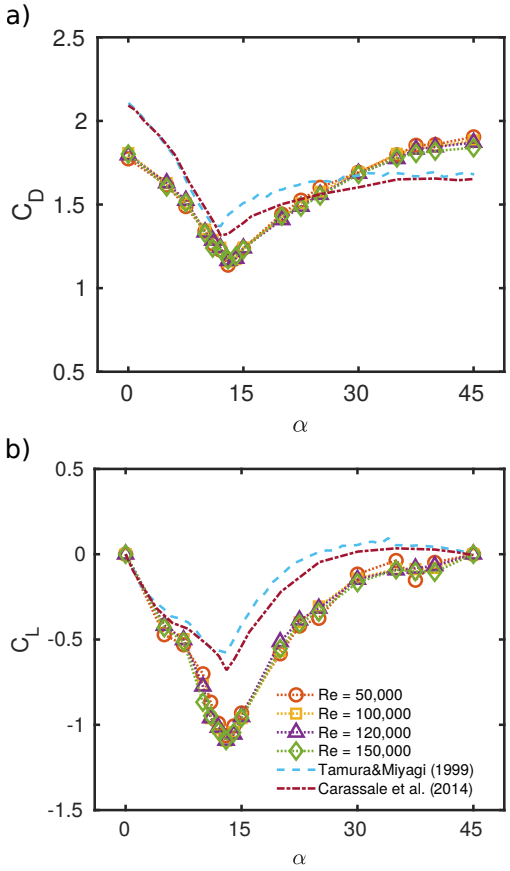

Figure 4: Mean aerodynamic force coefficients as a function of angle of attack. (a) mean drag coefficient; (b) mean lift coefficient. Data for the square cylinder from Tamura and Miyagi (1999) (Re=30,000) and from Carassale et al. (2014) (Re=37,000) was recalculated with projected frontal width for comparison purposes. (The legend in part b) applies to both parts of this figure)

The presence of extrema in the mean force coefficients at a certain angle of attack shows that critical behaviour, similar to that of the square cylinder, is also present in the cactus-shaped cylinder. The minimum value of C_D as well as maximum absolute value of the lift coefficient are attained at the same angle of attack $\alpha_{cr} = 13°$ (Figure 4).

3.2. Unsteady lift force

The time history of the lift force fluctuations was recorded at all tested angular positions for Reynolds number 100,000. The unsteady lift force coefficient (C'_L) is presented in Figure 5 as a function of angle of attack. The maximum value of C'_L is observed at zero angle of attack, followed by a reduction to its minimum value at $\alpha = 12°$. This value is slightly lower than α_{cr} obtained from the mean force coefficients. With further increase in α, the fluctuating lift force

coefficient recovers slightly and then remains close to constant over the range $15° \leq \alpha \leq 45°$.

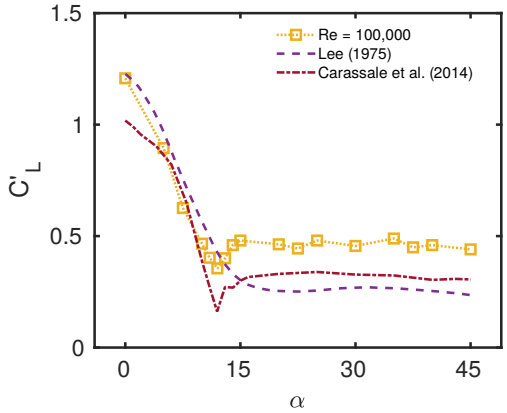

Figure 5: Unsteady lift force coefficient of the cactus-shaped cylinder as a function of angle of attack at Re = 100,000. Data for the square cylinder from Lee (1975) (Re=176,000) and from Carassale et al. (2014) (Re=37,000) was recalculated with projected frontal width for comparison purposes

Before comparing to the square cylinder it should be noted that there is a limited number of studies where C'_L dependence on the angle of attack is reported, since many studies on the square cylinder consider only the mean force coefficients. In addition, significant deviations between C'_L values reported in the literature can be observed (see Figure 5).

Overall, C'_L dependency on the angle of attack of the cactus-shaped cylinder follows the same trend as that of the square cylinder (Figure 5). Below the critical angle of attack a good match between the C'_L values for the two different shapes can be observed. At $\alpha = \alpha_{cr}$ reduction in fluctuating lift is higher in the square cylinder case (the minimum value of C'_L at α_{cr} is not captured in Lee (1975) because of the coarse steps in the angle of attack). At angles of attack above the critical, C'_L values of the cactus-shaped cylinder are consistently higher but also settle down to a constant value as observed for the square cylinder case.

3.3. Surface pressure distribution

As expected from the mean force data, no Reynolds number dependency was observed for the surface pressure distribution. In Figure 6 the variation of the time-averaged pressure coefficient around the cactus-shaped cylinder is presented at different angles of attack for Reynolds number 100,000. The pressure coefficient was determined from the experimental data as

$$C_p = \frac{p - p_\infty}{0.5\rho U_\infty^2} = \frac{p - p_\infty}{p_0 - p_\infty} \tag{2}$$

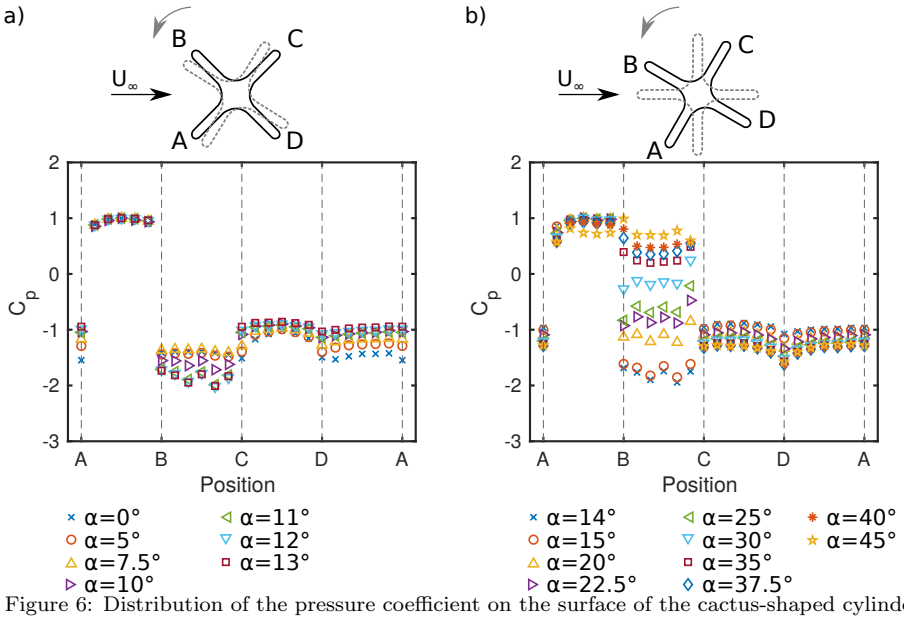

Figure 6: Distribution of the pressure coefficient on the surface of the cactus-shaped cylinder with four ribs at Re=100,000. a) angular orientations up to critical angle of attack ($\alpha = 0° - 13°$); b) angular orientations above critical angle of attack ($\alpha = 14° - 45°$)

where p is the static pressure at the point of measurement, p_∞ the static pressure in the freestream, and p_0 the freestream total pressure. The pressure distribution shows significant variation with angle of attack. Both for the 0° and 45° cases, a symmetric pressure distribution is recovered as expected for a cylinder with 4-fold symmetry. Since the front cavity (between points A and B) is always upstream for all tested angular orientations ($0° \leq \alpha \leq 45°$), the pressure coefficient inside shows positive values (Figures 6a and 6b). For the bottom (between points D and A) and rear (between points C and D) cavities the pressure coefficient has negative values at all angular positions. This can be explained by the fact that flow separating from rib A does not reattach to the surface of the bottom cavity at any angle of attack, and a recirculation zone is present downstream of the rear cavity. The pressure coefficient behaviour is more complex for the top cavity surface (between points B and C), showing negative values for angles of attack lower than 30°. For $\alpha > 30°$ the pressure coefficient inside the top cavity has positive values since at this orientation the front of rib C starts to be exposed to the flow.

As inferred from the mean force measurements, the critical angle for the cactus-shaped cylinder is attained at $\alpha_{cr} = 13°$. Focusing on the surface pressure coefficient distribution for angles below critical (see Figure 6a), it is observed that the pressure coefficient inside cavity AB shows negligible variation with angular orientation. While the absolute value of the pressure coefficient measured at the tip of rib A slightly decreases, a small increase of C_p is observed at the equivalent location at the tip of rib B. The maximum value of the pres-

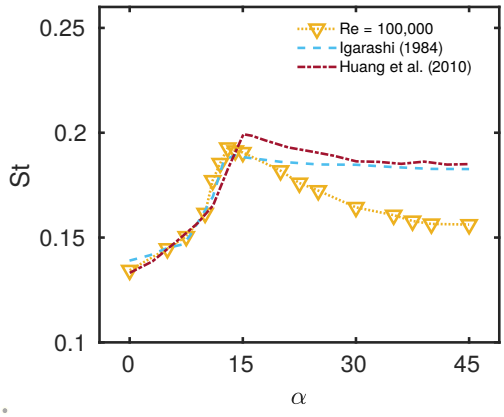

Figure 7: Strouhal number of the cactus-shaped cylinder with four ribs as a function of angle of attack. Data for the square cylinder from Igarashi (1984) (Re=37,000) and Huang et al. (2010) ($46,000 \leq \mathrm{Re} \leq 94,000$) is presented for comparison

sure coefficient inside cavity AB is observed at its centre and is close to unity. C_p inside cavities CD and DA and on tips of ribs C and D increases with angle of attack reaching maximum values at $\alpha = \alpha_{cr}$. The pressure coefficient inside cavity BC does not show significant variation for $0° \leq \alpha \leq 7.5°$. With further increase of angle of attack, the pressure inside this cavity drops, reaching its minimum at $\alpha = \alpha_{cr}$.

At critical angle of attack, the pressure coefficient inside the top cavity BC attains its absolute highest value while inside the opposite bottom cavity DA it reaches its absolute lowest value, thus maximizing the pressure difference. This explains the maximum lift force generated by the cactus-shaped cylinder at the critical angle of attack. Similarly, at α_{cr} the lowest absolute value of the pressure coefficient on the surface of the rear cavity CD contributes to the reduced drag at this angle of attack.

For angles of attack higher than critical (Figure 6b), the pressure coefficient inside cavity AB tends to show a small decrease in C_p with increasing α. Values of the pressure coefficient inside cavity BC and on rib tip B show a considerable increase with α reaching maximum values at $\alpha = 45°$. On the other hand, C_p inside cavities CD and DA and on rib tips C,D, and A decreases with α up to $\alpha = 37.5°$ and starts to recover at higher angles of attack.

3.4. Strouhal number

As for the mean force and surface pressure coefficients, no Reynolds number dependency is observed for the Strouhal number. St as a function of angle of attack at Reynolds number of 100,000 is presented in Figure 7. The value of the Strouhal number increases with α and reaches its maximum at $\alpha = 13°$. This matches the critical angle of attack observed in the mean force measurements. With further increase in the angle of attack up to $\alpha = 45°$, the Strouhal number gradually decreases.

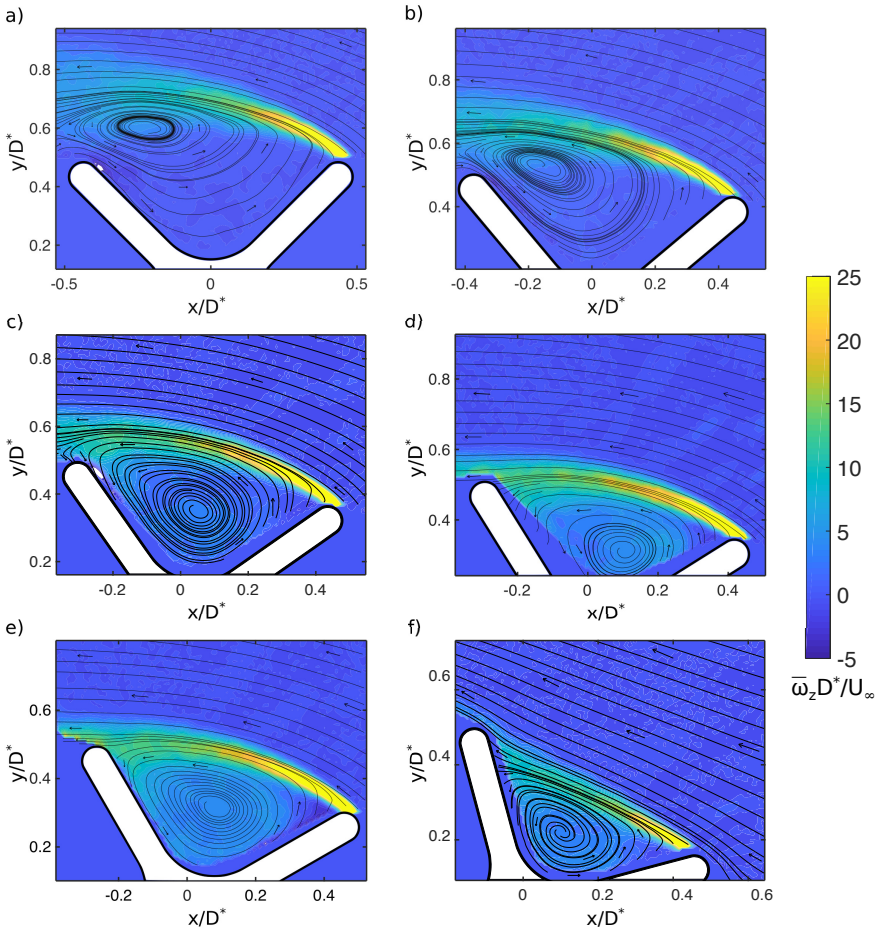

Figure 8: Contours of the mean vorticity fields and mean flow streamlines around the top part of the cactus-shaped cylinder with four ribs at Re=50,000. a) $\alpha = 0°$; b) $\alpha = 5°$; c) $\alpha = 10°$; d) $\alpha = 13°$; e) $\alpha = 15°$; f) $\alpha = 30°$. The freestream velocity is in the negative x-direction

For comparison, data on St of the square cylinder (Igarashi, 1984; Huang et al., 2010) is also presented in Figure 7. Up to the critical angle of attack, the Strouhal numbers of both shapes follow the same increasing trend and have closely matched values. However, at angles of attack above the critical the cactus-shaped cylinder has lower values of St compared to the square cylinder and this difference increases with α.

3.5. Quantitative flow visualisations

To gain further insight into the flow patterns and reattachment behaviour of the cactus-shaped cylinder PIV measurements were performed around its top part. Contours of the mean vorticity with superimposed mean flow streamlines are shown in Figure 8 for six angles of attack. For all tested angular orientations

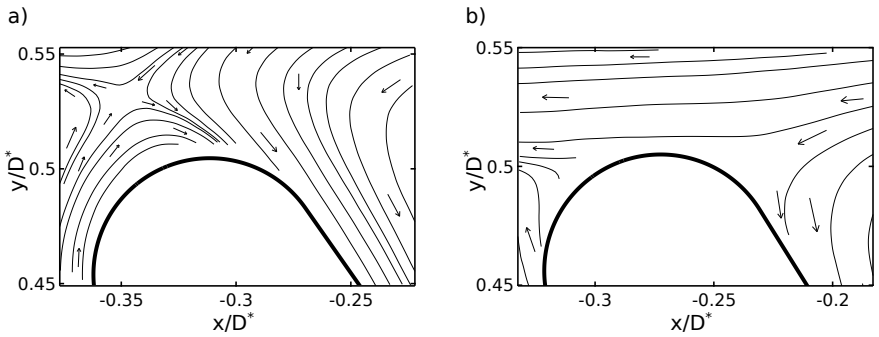

Figure 9: Mean flow streamlines around the back rib of the cactus-shaped cylinder with four ribs at Re=50,000. a) $\alpha = 10°$; b) $\alpha = 13°$. The freestream velocity is in the negative x-direction

separation of the shear layer from the front rib is observed. In addition, a recirculation bubble is formed inside the cavity between the front and back ribs. The separated mean shear layer follows the boundary of this recirculation bubble and $\overline{\omega_z}$ is decreasing in the downstream direction.

In the range $0 \leq \alpha < 13°$ (see Figure 8a-c), the separated shear layer moves closer to the tip of the back rib with increasing angle of attack, but no reattachment is observed. The size of the recirculation bubble decreases with increasing α and its centre shifts more deeply inside the cavity. At angle of attack of 13°, i.e. the critical angle, the separated shear layer reattaches to the back rib of the cactus-shaped cylinder and the recirculation bubble becomes fully enclosed inside the cavity. This is more clearly demonstrated in Figure 9 where mean flow streamlines are presented in a close up view in the region around the back rib at two angular orientations of 10° and 13°. At $\alpha = 10°$ (Figure 9a) no reattachment at the back rib is observed, while with an increase of α to 13° (Figure 9b) the reattachment occurs. This angular orientation of 13° corresponds to the critical angle of attack that was observed in the mean force coefficients and Strouhal number data. In addition, the critical angle of attack separates two distinctive flow regimes around the cactus-shaped cylinder, namely perfect separation and reattachment, that are also distinguished in the square cylinder case (Igarashi, 1984). Reattachment of the shear layer is observed with the increase of α above the critical value (see Figure 8e, f). Moreover, the length of the reattachment zone on the back rib expands towards the centre of the cavity with an increase in angle of attack, while the size of recirculation bubble inside the cavity decreases.

3.6. Critical angle of attack

As discussed in the previous sections, a critical angle of attack α_{cr} is present for the studied cactus-shaped cylinder where C_D and C'_L attain their minimum values, while C_L and St reach maxima. While mean aerodynamic coefficients and Strouhal number reach their extrema at $\alpha = 13°$, the fluctuating lift coefficient attains its lowest value at a slightly lower angle of $\alpha = 12°$. Similar

dispersion of the critical angle values of attack was observed for the square cylinder (see Table 1), where reported values of α_{cr} are between 12° and 15°. As in the case of the square cylinder, critical behaviour of the studied cactus-shaped cylinder is associated with the reattachment of the shear layer, which separates from the front rib, to the the back rib and which was confirmed by the flow visualisations discussed in the previous section. Modifications to the corners of the square cylinder are known to have a strong influence on the reattachment of separated shear layers, and tend to shift the critical angle of attack to lower values (Tamura and Miyagi, 1999; Carassale et al., 2014) (see Table 1). This effect is not observed in case of the cactus-shaped cylinder, where the critical angle of attack is in the range reported for the square cylinder.

Table 1: Overview of the extreme values of aerodynamic coefficients and Strouhal number at critical angle of attack for cactus-shaped cylinder and previously reported data on the square cylinder

	Re	$C_{D\min}(\alpha_{cr})$	$\lvert C_L\rvert_{\max}(\alpha_{cr})$	$C'_{L\min}(\alpha_{cr})$	$St_{\max}(\alpha_{cr})$
Present case	100,000	1.138(13°)	1.064(13°)	0.187(12°)	0.192(13°)
Square cylinder					
Lee (1975)	176,000	1.26(12°)	0.67(13°)	-	0.18(15°)
Igarashi (1984)	56,000	1.36(14°)	0.64(14°)	-	0.19(14°)
Tamura and Miyagi (1999)	30,000	1.37(12°)	0.60(13°)	0.15(11°)	0.18(15°)
Carassale et al. (2014)	37,000	1.32(12°)	0.68(13°)	0.16(12°)	0.18(14°)
Square cylinder with modified corners					
Tamura and Miyagi (1999)*	30,000	0.80(5°)	0.64(5°)	0.15(4°)	0.22(5°)
Tamura and Miyagi (1999)**	30,000	1.02(7°)	0.28(8°)	0.13(6°)	0.21(7°)
Carassale et al. (2014)***	27,000	1.28(8°)	0.61(9°)	0.13(8°)	0.19(9°)
Carassale et al. (2014)****	27,000	1.10(6°)	0.57(7°)	0.15(5°)	0.20(7°)

If necessary, force coefficients and Strouhal numbers from the literature were recalculated with the projected frontal area and projected side length respectively for comparison purposes.
* - square cylinder with rounded corners, $r = D/6$,
** - square cylinder with chamfered corners, $size = D/6$,
*** - square cylinder with rounded corners, $r = D/15$,
**** - square cylinder with rounded corners, $r = D/7.5$,
where r - radius of the corner rounding

3.7. Power spectra

The power spectral density (E_u) of the streamwise component of the velocity based on hot-wire measurements at two downstream positions behind the cactus-shaped cylinder is shown in figure (Figure 10) for four angles of attack at Reynolds number 100,000. The first position was located at $x = 2.5D$ downstream of the centre of the cylinder with cross-stream offset $y = 2.5D$ with respect to the centreline, and the second position at $x = 6.5D$ using the same

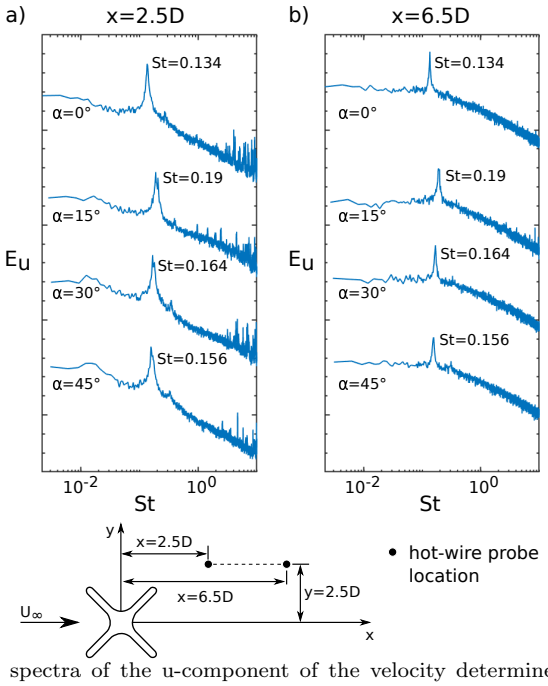

Figure 10: Power spectra of the u-component of the velocity determined for four angular orientations at two locations behind the cactus-shaped cylinder at Re=100,000. a) $x = 2.5D$, $y = 2.5D$ b) $x = 6.5D$, $y = 2.5D$. The scale on the vertical axis is arbitrary but the same scale is used for each spectrum. For clarity, the spectra have been shifted relative to each other along the vertical axis

cross-stream offset. The data was averaged with Bartlett's method using 16 segments. The ordinate axis in Figure 10 has arbitrary scale but the same scale was used for all presented spectra for comparison purposes.

At both locations ($x = 2.5D$ and $x = 6.5D$) a dominant peak in E_u is present for all angles of attack. These peaks indicate spanwise vortex shedding and correspond to the Strouhal numbers of the cactus-shaped cylinder at these particular angular orientations. In addition, in all cases at least one higher harmonic can be observed. At intermediate angles of attack ($\alpha = 15°$ and $\alpha = 30°$, a further peak can be observed that is close to the primary one. This can be attributed to secondary vortex shedding at these angles of attack. Similar behaviour was previously observed in a URANS-based investigation of a cactus-shaped cylinder with four ribs (Zhdanov and Busse, 2019).

3.8. Comparison with earlier 2D URANS results

In the present section, the current experimental results are compared to an earlier 2D URANS-based investigation of the same cactus-shaped cylinder at a Reynolds number of 20,000 (Zhdanov and Busse, 2019). Whilst this previous investigation was at a Reynolds number below the range studied in the experiments, a comparison of results obtained at different Re can be justified by the

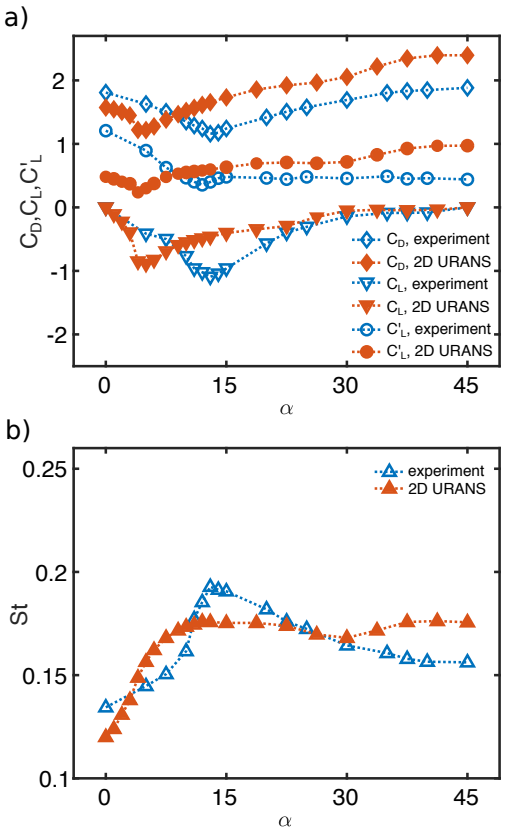

Figure 11: Aerodynamic force coefficients and Strouhal number as a function of an angle of attack obtained from the present experiments at representative Reynolds number of 100,000 compared to the URANS results (Zhdanov and Busse, 2019) for the same shape at Reynolds number of 20,000. (a) Force coefficients; (b) Strouhal number

similarities of the aerodynamic behaviour between the studied shape and the square cylinder. The cactus-shaped cylinder does not exhibit Re dependence within the range of 50,000 to 150,000, and in investigations of the square cylinder no Reynolds number dependence is observed at $Re > 1,000$ (Bai and Alam, 2018). Therefore, it can be reasonably presumed that no significant changes would be observed at $Re = 20{,}000$.

Both experimental and 2D URANS investigations capture the presence of the critical angle of attack for the studied cactus-shaped cylinder, but its actual value is underpredicted by the 2D URANS simulations. In both experiments and URANS simulations α_{cr} is associated with the reattachment of the separated shear layer from the front rib to the back rib. Qualitatively, experimental and 2D URANS results demonstrate the same trends in the behaviour of aerodynamic coefficients and Strouhal number with angle of attack (Figure 11). With the change of α from 0° up to the critical angle, values of C_D and fluctuating lift coefficient decrease to their minima, whilst St and the absolute value of C_L

increase and reach their maxima. With further increase of the angle of attack from α_{cr} to 45° an increase in the mean drag coefficient is observed, while C'_L attains an approximately constant value after an initial increase. The Strouhal number and absolute mean lift coefficient decrease over the same range. A mismatch in the behaviour of St and C'_L between experimental and 2D URANS results is present at angles of attack $> 30°$.

At most angular orientations, quantitative differences are observed for the aerodynamic coefficients and Strouhal number when comparing experimental and URANS results (Figure 11), which can be related to the underprediction of the critical angle of attack by the 2D URANS simulations. Fairly good quantitative agreement is observed for the mean lift coefficient at angles of attack up to 4° and at $\alpha > 22.5°$ (Figure 11a).

The observed quantitative differences between experimental results and 2D URANS simulations are in line with conclusions of the work of Mannini et al. (2010), who studied URANS modelling of the flow past a rectangular cylinder: the quantitative match tends to be better at $\alpha = 0°$ compared to a finite angle of attack. In addition, the URANS simulations are able to predict the physical behaviour found in the experiments in a qualitative way, but for unsteady bluff-body flows 2D URANS has limited accuracy. Overall, the 2D URANS approach provides useful insight into key features of the flow past a cactus-shaped cylinder, but for a close quantitative agreement to experimental data 3D eddy-resolved methods, e.g. Large-Eddy Simulations, are required.

4. Conclusions

An experimental investigation of the aerodynamic properties of a cactus-shaped cylinder with four ribs was conducted in low speed wind tunnels. The studied shape is a modification to the cross section of a square cylinder inspired by a number of tall succulents that have four ribs. The cactus-shaped cylinder showed strong angle of attack dependence of aerodynamic coefficients and Strouhal number. No Reynolds number dependence was observed within the tested range from 50,000 to 150,000.

With an increase of the angle of attack, reduction of the mean drag and fluctuating lift coefficients was observed, while Strouhal number and the absolute value of the lift coefficient were found to increase. At angle of attack of 13° C_D reached its minimum, and $|C_L|$ and St reached their maxima. The highest reduction in C'_L was observed at $\alpha = 12°$. Taking into account previous studies on square cylinders, a critical angle of attack exists for the studied cactus-shaped cylinder between 12° and 13°. Similar to the square cylinder, the critical behaviour is caused by a reattachment of the shear layer that separates at the front rib to the back rib as was confirmed by quantitative flow visualisations using PIV. These observations are also supported by the mean surface pressure distribution at this angle of attack, which showed the highest pressure difference between top and bottom cavities, resulting in the maximum lift coefficient value. In addition, at the critical angle the absolute lowest C_p was recorded inside the rear cavity contributing to the lowest drag.

Previous studies on the square cylinder with modified corners found a shift of the critical angle of attack towards lower values compared to the square cylinder. This effect was not observed in the present study where α_{cr} of the cactus-shaped cylinder falls within the reported range of the square cylinder. This could be attributed to the small tip radius of the ribs as well as to the effect of large vortices trapped in the side cavities.

Comparing values of the aerodynamic coefficients of the cactus-shaped cylinder to those of the square cylinder a reduction of the mean drag was observed for $\alpha \leq 30°$. The mean lift coefficient was higher for the studied shape at all angles of attack except for the two extreme orientations where mean lift vanishes due to the symmetry. At angles of attack below critical, both C'_L and St showed similar values to those of the square cylinder. Moreover, a reduction in Strouhal number was observed with further increase in α.

Studies on Saguaro-inspired cylinders with many ribs demonstrated their ability to reduce drag and unsteady lift fluctuations, thus helping Saguaro cacti to deal with aerodynamic loads in their environment. The present study on a succulent-inspired cylinder with four ribs suggests that this shape also provides aerodynamic benefits to actual plants albeit over a limited range of angular orientations. Typically, natural evolution is a result of a competition between various biotic and abiotic factors that affect survival and development of an organism. In complex living systems, like plants, the minimum requirement for their survival and normal functioning is usually determined by a single factor that limits the development of other functions and features (Niklas, 1992). Therefore, while aerodynamics may be one of the factors driving the adaptation of succulents to their environment, it is probably not the critical one and other factors, e.g. heat transfer and water collection and retention may be more dominant.

In the current succulent-inspired study, as well as in previous investigations on cacti with many ribs (Talley et al., 2001; Wang et al., 2014; Letchford et al., 2016), the plant geometry was simplified to a 2D cylinder as the focus was on the aerodynamic influence of the plant's ribs. However, cacti and succulents exhibit further features that may influence their aerodynamics, such as ridges, spines, and branches. In future studies, these elements could be successively added to explore their potential to further enhance the aerodynamic properties of these plants.

Acknowledgements

The authors gratefully acknowledge access to the low-speed National Wind Tunnel Facility funded by the Engineering and Physical Sciences Research Council, grant number EP/L024888/1, and support by the University of Glasgow's Lord Kelvin/Adam Smith (LKAS) PhD scholarship scheme.

References

Achenbach, E., 1971. Influence of surface roughness on the cross-flow around a circular cylinder. Journal of Fluid Mechanics 46, 321–335. doi:10.1017/S0022112071000569.

Apelt, C., West, G., Szewczyk, A.A., 1973. The effects of wake splitter plates on the flow past a circular cylinder in the range $10^4 < \mathrm{R} < 5 \times 10^4$. Journal of Fluid Mechanics 61, 187–198. doi:10.1017/S0022112073000649.

Bai, H., Alam, M.M., 2018. Dependence of square cylinder wake on Reynolds number. Physics of Fluids 30, 015102. doi:10.1063/1.4996945.

Bearman, P., Trueman, D., 1972. An investigation of the flow around rectangular cylinders. The Aeronautical Quarterly 23, 229–237. doi:10.1017/S0001925900006119.

Bushnell, D.M., Moore, K., 1991. Drag reduction in nature. Annual Review of Fluid Mechanics 23, 65–79. doi:10.1146/annurev.fl.23.010191.000433.

Carassale, L., Freda, A., Marre-Brunenghi, M., 2014. Experimental investigation on the aerodynamic behavior of square cylinders with rounded corners. Journal of Fluids and Structures 44, 195–204. doi:10.1016/j.jfluidstructs.2013.10.010.

Cheng, W., Pullin, D., Samtaney, R., 2018. Large-eddy simulation of flow over a grooved cylinder up to transcritical Reynolds numbers. Journal of Fluid Mechanics 835, 327–362. doi:10.1017/jfm.2017.767.

Choi, H., Park, H., Sagong, W., Lee, S.i., 2012. Biomimetic flow control based on morphological features of living creatures. Physics of Fluids 24, 121302. doi:10.1063/1.4772063.

Green, R.B., Gillies, E.A., Brown, R.E., 2005. The flow field around a rotor in axial descent. Journal of Fluid Mechanics 534, 237–261. doi:10.1017/S0022112005004155.

Hanke, W., Witte, M., Miersch, L., Brede, M., Oeffner, J., Michael, M., Hanke, F., Leder, A., Dehnhardt, G., 2010. Harbor seal vibrissa morphology suppresses vortex-induced vibrations. Journal of Experimental Biology 213, 2665–2672. doi:10.1242/jeb.043216.

He, G.S., Li, N., Wang, J.J., 2014. Drag reduction of square cylinders with cut-corners at the front edges. Experiments in Fluids 55, 1745. doi:0.1007/s00348-014-1745-1.

Hu, J., Zhou, Y., Dalton, C., 2006. Effects of the corner radius on the near wake of a square prism. Experiments in Fluids 40, 106. doi:10.1007/s00348-005-0052-2.

Huang, R., Lin, B., Yen, S., 2010. Time-averaged topological flow patterns and their influence on vortex shedding of a square cylinder in crossflow at incidence. Journal of Fluids and Structures 26, 406–429. doi:10.1016/j.jfluidstructs.2010.01.003.

Igarashi, T., 1984. Characteristics of the flow around a square prism. Bulletin of JSME 27, 1858–1865. doi:10.1299/jsme1958.27.1858.

Kawall, J., Shokr, M., Keffer, J., 1983. A digital technique for the simultaneous measurement of streamwise and lateral velocities in turbulent flows. Journal of Fluid Mechanics 133, 83–112. doi:10.1017/S0022112083001809.

Lee, B., 1975. The effect of turbulence on the surface pressure field of a square prism. Journal of Fluid Mechanics 69, 263–282. doi:10.1017/S0022112075001437.

Letchford, C., Lander, D., Case, P., Dyson, A., Amitay, M., 2016. Bio-mimicry inspired tall buildings: The response of cactus-like buildings to wind action at Reynolds number of 10^4. Journal of Wind Engineering and Industrial Aerodynamics 150, 22–30. doi:10.1016/j.jweia.2016.01.001.

Mannini, C., Šoda, A., Schewe, G., 2010. Unsteady RANS modelling of flow past a rectangular cylinder: Investigation of Reynolds number effects. Computers & fluids 39, 1609–1624. doi:10.1016/j.compfluid.2010.05.014.

McGhee, G.R., 2011. Convergent evolution: limited forms most beautiful. MIT Press.

Naudascher, E., Weske, J., Fey, B., 1981. Exploratory study on damping of galloping vibrations. Journal of Wind Engineering and Industrial Aerodynamics 8, 211–222. doi:10.1016/0167-6105(81)90020-9.

Niklas, K.J., 1992. Plant biomechanics: an engineering approach to plant form and function. University of Chicago press.

Talley, S., Iaccarino, G., Mungal, G., Mansour, N., 2001. An experimental and computational investigation of flow past cacti. Annual Research Briefs, Center for Turbulence Research, NASA Ames/Stanford University , 51–63.

Tamura, T., Miyagi, T., 1999. The effect of turbulence on aerodynamic forces on a square cylinder with various corner shapes. Journal of Wind Engineering and Industrial Aerodynamics 83, 135–145. doi:10.1016/S0167-6105(99)00067-7.

Wang, S., Liu, Y., 2016. Wake dynamics behind a seal-vibrissa-shaped cylinder: A comparative study by time-resolved particle velocimetry measurements. Experiments in Fluids 57, 32. doi:10.1007/s00348-016-2117-9.

Wang, S.F., Liu, Y.Z., Zhang, Q.S., 2014. Measurement of flow around a cactus-analogue grooved cylinder at $Re_D = 5.4\times10^4$: Wall-pressure fluctuations and flow pattern. Journal of Fluids and Structures 50, 120–136. doi:10.1016/j.jfluidstructs.2014.06.019.

Zhdanov, O., Busse, A., 2019. Angle of attack dependence of flow past cactus-inspired cylinders with a low number of ribs. European Journal of Mechanics-B/Fluids 75, 244–257. doi:10.1016/j.euromechflu.2018.09.008.